Effect of supporting electrolyte concentration on one-step electrodeposited $CuInS_2$ films for ZnS/$CuInS_2$ solar cell applications

C. A. Rodríguez[a,b,*], A. Delgadillo[b], J. Nuñez[c], G. Cabello-Guzmán[d], Adriana C. Mera[a,b], M. P. Delplancke[e], B. Villacampa[f] and C. Carrasco[c]

[a] *Multidisciplinary Research Institute for Science and Technology, Universidad de La Serena, 1015 Juan Cisternas Av., La Serena, Chile*

[b] *Department of Chemistry, Faculty of Sciences, University of La Serena, Campus Andrés Bello, 1305 Raúl Bitrán Av., La Serena, Chile*

[c] *Thin Films and Electrochemical Process Laboratory, Departamento de Ingeniería de Materiales, Universidad de Concepción, Edmundo Larenas 270, Concepción, Chile*

[d] *Department of Basic Sciences, Faculty of Sciences, University of Bío-Bío, Campus Fernando May, Chillán, Chile*

[e] *4MAT, Université Libre de Bruxelles, 50 Roosvelt Av., CP 165/63, Brussels 1050, Belgium*

[f] *Department of Condensed Matter Physics, ICMA, Universidad de Zaragoza-CSIC, 50009, Zaragoza, Spain*

*Corresponding author. E-mail address: arodriguez@userena.cl. Tel.: +56-51-233 4881

Abstract

A one-step electrodeposition process is used to obtain $CuInS_2$ (CIS) films on a molybdenum substrate by varying the supporting electrolyte (lithium chloride, LiCl) concentration. The as-deposited samples are characterized by scanning electron microscopy, energy dispersive spectroscopy, profilometry and diffuse reflectance spectroscopy. It is found that different concentrations of LiCl mainly lead to a morphological change and that the chemical composition of the obtained CIS films shifts to the stoichiometric composition for high concentrations of supporting electrolyte. After annealing, the structural analysis from X-ray diffraction reveals that all samples crystallized in the tetragonal phase of CIS. In addition, it is found that the crystallite size increased for samples grown at higher concentrations of LiCl. Optical studies carried out by diffuse reflectance spectroscopy reveal that the band gap values increase from ~1.40 to ~1.45 eV (average) after the annealing process. Finally, zinc sulfide (ZnS) thin films are chemically deposited onto electrodeposited CIS films in order to evaluate the photovoltaic response of ZnS/CIS bilayer systems. We discover that ZnS thin films cover the surface of CIS more effectively for the highest concentration of LiCl and that only the ZnS/CIS bilayer with the CIS film obtained at the highest concentration of LiCl shows a photovoltaic response.

Keywords: $CuInS_2$ films, electrodeposition, electrolyte; thin film solar cells

1. Introduction

$CuInS_2$ (CIS) is a ternary semiconductor with excellent potential as an absorbent material for thin film solar cells (TFSCs) [1–5]. Experimentally, CIS-based solar cells exhibit a limited energy conversion efficiency when compared with other chalcopyrite ternary semiconductor-based photovoltaic devices, such as $CuXSe_2$ (X = In, Ga) and $Cu(In,Ga)Se_2$ [6–7]. However, the low cost and toxicity of CIS make it a promising candidate as an absorbent layer in solar cells.

Although the highest efficiency currently achieved for CIS-based solar cells is only 13% [8], there is still potential to continue increasing the conversion efficiency based on the optical properties of the material and its theoretical energy conversion efficiency of 32% [9]. CIS has a direct band gap of ~1.5 eV and a high absorption coefficient (10^5 cm^{-1}), which ensures absorption of most of the visible solar spectrum [10,11]. This compound also has good radiation stability and environmental compatibility, which should allow CIS photovoltaic devices to maintain performance even in adverse conditions [12].

So far, several methods, such as co-evaporation, sputtering, spray pyrolysis and electrodeposition, have been used for the fabrication of CIS thin films [13–15]. Among these methods, co-evaporation and sputtering are the most used to synthesize CIS films for TFSC applications. However, expensive equipment is needed for vacuum environments and high purity targets must be used in these deposition techniques. Therefore, these two methods are expensive for the production of large-area CIS thin films. In contrast, electrodeposition is an attractive method that can be used to fabricate large-area thin films at a lower cost.

Currently, there are two routes for the electrodeposition of CIS: one- and two-step routes [10,16,17]. In the two-step route, a layer of Cu-In is deposited first and the layer is then subjected to a thermal sulfurization process to form CIS. Accordingly, in the two-step

route, the procedure becomes more complicated and the subsequent sulfurization process at high temperature requires the usage of a H_2S or S atmosphere, which are harmful, corrosive and flammable [2,18]. In the one-step route, a sulfur source (commonly sodium thiosulfate) with metallic copper and indium ions are deposited simultaneously on the substrate surface. Since greener fabrication processes are increasingly required, efforts to exclude H_2S throughout the synthesis of semiconductor thin films have to be utilized [2,19,20]. Thus, the one-step electrodeposition process has arisen as a less toxic, simpler and cheaper route to fabricate large-area CIS thin films.

The effect of different experimental conditions on the one-step electrodeposition of CIS films has been thoroughly investigated. So far, the influence of deposition time [17], concentration of precursors [21], applied potential [22] and complexing agents [2] has been studied. However, the effect of supporting electrolyte concentration on one-step electrodeposited CIS film properties has so far not been addressed.

Supporting electrolytes are normally used during electrodeposition of a film to increase the conductivity of the solution and to keep the ionic strength and pH constant [23]. It has been shown that increasing the concentration of the supporting electrolyte leads to an increase in the values of minimum activation resistance of the electrode reaction and a decrease in the standard rate constants of the first electroreduction step [24]. Accordingly, film properties can be affected and modified by varying the supporting electrolyte concentration. The usage of supporting electrolytes has been widely reported for the one-step electrodeposition process because it favors codeposition [25]. Chloride- and sulfate-based electrolytes are the most used for electrodeposition [2,25–27]; however, in acidic conditions, sulfate-based electrolytes are not sufficiently inert, resulting in reduction to $SO_{2(g)}$. Accordingly, LiCl has been widely used as a support electrolyte in one-step electrodeposited CIS films [2,19,28,29].

In this work, CIS films are fabricated through a one-step electrodeposition method. The effect of the supporting electrolyte concentration on the morphological characteristics, chemical composition and the optical and structural properties of the CIS films are analyzed. Furthermore, ZnS/CIS bilayers are fabricated using the one-step electrodeposited CIS films, in order to investigate their ability as absorbent layers in TFSCs. The morphological characteristics, chemical composition and photovoltaic response of the bilayers are reported.

2. Experimental

2.1 Polarization curves and electrodeposition of CIS

Prior to the deposition process, in order to investigate the effect of the supporting electrolyte concentration on the reduction potential of CIS, potentiodynamic measurements were performed. An Amel 2549 potentiostat/galvanostat in a three-electrode cell configuration was used. A molybdenum (Mo) foil with an exposure surface of 0.5 cm × 0.5 cm, a platinum wire and a saturated calomel electrode (SCE) were used as the working, counter and reference electrodes, respectively. Mo substrates (Sigma-Aldrich, 99%, 0.1 mm thick) were cleaned with soap and rinsed with distilled water and alcohol. Subsequently, the Mo substrate was dried at room temperature.

The electrolytic bath contained 7.8 mmol $CuCl_2$, 6.25 mmol $InCl_3$, 23 mmol $C_8H_5KO_4$ (KHP), 23.4 mmol $Na_2S_2O_3$ and X mmol LiCl (X = 50, 100, 150, 200 or 250). The metallic sources, complexing agent and source of the sulfur ions were kept constant, while the LiCl concentration added to the electrolytic bath was changed, resulting in five different electrolytic baths. The pH was adjusted to 2.5 by adding diluted HCl and the bath temperature was kept constant at 30 °C. The electrolytic bath was deaerated with N_2 gas for 20 min to remove any dissolved oxygen in the solution. The potentiodynamic

curves were scanned from 0 to -1.8 V vs. SCE with a constant scan rate of 10 mVs^{-1}. Polarization curves for each individual ionic specie were also performed; It should be noted that the main findings are similar to the reported elsewhere [2], reason why they are not shown here.

The electrodeposition process for CIS thin films was carried out potentiostatically following the same experimental details for the polarization curves. The one-step electrodeposition process was started by applying a constant potential of −1 V vs. SCE for 30 min. Then, the electrodeposited samples were removed from the solution and cleaned with distilled water to remove any non-well-adhered material and dried at room temperature. All the obtained CIS thin films were uniformly dark and well covered the surface substrate. The as-deposited samples were labelled as CIS–X, where X = 50, 100, 150, 200 or 250 mmol, which represented the LiCl concentrations added to the electrolytic bath, respectively. Finally, the deposited films were annealed in a 95% N_2 + 5 % H_2 atmosphere for 1 h at 400 °C . Before heating, air was purged for 90 min and then the program was started with a heating rate of 10 °C/min. The annealed samples were labelled by adding the letter 'a' to the previously defined labels (a–CIS–X).

For all the as-deposited samples, the morphological characteristics and chemical composition were investigated by scanning electron microscopy (SEM, Hitachi Su 70) coupled with energy dispersive spectroscopy (EDS). The film thickness was measured using a Bruker Stylus profiler model Dektak XT. The optical properties were studied by means of diffuse reflectance spectroscopy using an ultraviolet-visible spectrophotometer ThermoScientific Evolution 220 with an integrating sphere for solid samples. The band gap values were estimated at the wavelength where a sharp increase in reflectance was observed [30]. After the annealing process of the CIS films, the measurements of the surface characteristics, EDS and optical band gap were carried out again. In addition, the

structural properties were measured by means of X-ray diffraction (XRD) using a D5000 Bruker diffractometer with Cu Kα radiation at 40 kV and 40 mA.

2.2 ZnS/CIS heterojunction

In order to investigate the ability of the one-step electrodeposited CIS films as absorbent materials in solar cells, three different ZnS/CIS bilayers are fabricated. A schematic representation of the fabrication of the ZnS/CIS/Mo solar cells is shown in Figure 1. For construction of the solar cells, after electrodeposition of CIS on the Mo substrate (see Fig. 1(a)), the ZnS thin film was chemically deposited on the obtained CIS layer. The solution for depositing the ZnS thin film has been reported elsewhere [31]. Once the non-toxic solution was prepared and the pH adjusted to 10.5 (total volume of 100 mL), CIS/Mo substrates were immersed in the reactor (see Fig. 1(b)). Subsequently, the reactor was transferred to a thermoregulated bath for 90 min at 75 °C. After this time, samples were removed from the solution, rinsed with deionized water and dried at room temperature. The upper Sn contact was made using a hot ultrasonic soldering unit model Sunbonder USM-5 from Kuroda Techno Co., Ltd. (see Fig. 1(c)).

The morphological characteristics of the obtained ZnS/CIS bilayers were investigated by field emission SEM (MERLIN^{TM} Carls Zeiss). The semi-quantitative chemical composition was measured by EDS attached to SEM. Finally, the photovoltaic response was measured using a solar simulator (Abet Technologies model 10500) as an irradiating source at 1 sun of irradiating power (1 sun = 1000 W/m^2) and a 2401 Source Meter Instrument (Keithley). A silicon reference cell equipped with a KG5 filter was used.

3. Results and discussion

3.1 Cathodic polarization curves

In order to study the effect of the concentration of LiCl on the reduction process of ions to form CIS, cathodic polarization curves were measured. Figure 2 shows the cathodic polarization curves for electrolytic baths with different concentrations of LiCl as a supporting electrolyte. The solution pH was adjusted to 2.5 by adding appropriate amounts of HCl. KHP was used as an effective complexing agent to bring the reduction potentials of Cu^{2+} and In^{+} closer [2]. Cathodic polarization curves for each ionic species are not included because they can be found elsewhere [2].

In Fig. 2, it is seen that the polarization curves exhibit similar behavior for all the different LiCl concentrations. Three clear reduction peaks can be observed and are located at –0.62, –0.90 and –1.1 V vs. SCE. The first peak is attributed to the reduction of Cu^{2+} to Cu^{+} and In^{3+} to In^{+} [2,21]. The second one is ascribed to the reduction of In^{+} to In^{0} [2] and the last one corresponds to the formation of $Cu_xIn_yS_z$ species (due to the reduction of Cu^{+} to Cu^{0} and In^{+} to In^{0}) [2]. In addition, the slight drop in the current density between –0.70 and –0.85 V vs. SCE can be attributed to the reduction of $S_2O_3^{2-}$ to S^{0} and S^{0} to S^{2-} [2,21].

Concerning the effect of the LiCl concentration, it can be clearly seen that as the LiCl concentration increases from 50 to 250 mmol, the reduction potential for the formation of $Cu_xIn_yS_z$ species shifts to more positive potentials, from –1.17 to –1.05 V vs. SCE. Nieszporek et al. suggested that the easier reduction of ionic species as the supporting electrolyte concentration increases is caused by a diminution of the hydration level of metallic ions, as well as the number of water molecules at the electrode surface [24]. In addition, it was experimentally observed that applied potentials more negative than –1 V vs. SCE results in inhomogeneous films, even for slightly more negative potentials (such

as –1.05 V vs. SCE) . In this sense, the applied potential to deposit the CIS film was set at –1 V vs. SCE.

3.2 Characterization of as-deposited samples

As-deposited samples were first characterized by SEM and EDS to select the CIS films, which exhibit morphological characteristics and chemical compositions similar to the stoichiometric characteristics and compositions, to be used as an absorbent layer in solar cells. Figure 3 shows the SEM images for as-deposited CIS films grown at different concentrations of LiCl. The films exhibit a dense and uniform surface with well-defined particles. It can be also observed that the morphology of the CIS samples is affected by the concentration of the supporting electrolyte. For sample CIS–50, irregular-shaped particles with agglomerates of ~1 μm are observed. A noticeable change in morphology is observed for sample CIS–100, where a compact layer is obtained on which agglomerates with larger sizes are seen (up to 2 μm). The agglomerates clearly tend to grow up to ~3.5–4.0 μm as the concentration of LiCl increases from 150 to 250 mmol. The presence of agglomerates at the surface in the electrodeposited CIS films has been reported previously [2,21]. Additionally, the measured thickness for all obtained CIS films produced was 2–3 μm (see Fig. 3(f)) and no clear trend was observed as a function of the LiCl concentration.

Table 1 shows the EDS results for as-deposited samples, where it is clear that the composition for sample CIS–50 is quite far from the stoichiometric ratio and a high atomic concentration of In and S was obtained. This is because the reduction potential for the $Cu_xIn_yS_z$ species with 50 mmol LiCl is less negative than –1 V vs. SCE (see Fig. 1), resulting in a favorable deposition of In_xS_y on the Mo surface.

For CIS-100, the atomic concentration of Cu increased as a result of the shift to a less negative reduction potential for $Cu_xIn_yS_z$ species. For the other samples, the Cu/In ratio is closer to the stoichiometric composition for CIS (i.e. 1); however, a slightly lower atomic concentration of S was obtained, where S/(Cu+In) is always below 1. The lower sulfur content in the one-step electrodeposited CIS films has also been reported previously [9].

Figure 4 shows the diffuse reflectance spectra of the as-deposited CIS films obtained at different concentrations of LiCl. From the spectra, a sharp increase in diffuse reflectance at wavelengths above 850 nm is observed, which agrees well with the absorption edge of the CIS films. As shown in Fig. 4, the edge is shifted from 876 to 894 nm as the concentration of the supporting electrolyte increases, leading to a slight reduction in the band gap values from 1.41 to 1.38 eV, all of which are in good agreement with those reported previously for CIS films [32,33].

From the above characterization, it can be observed that the optical properties of the obtained films are not strongly affected by the LiCl concentration; however, CIS–150, CIS–200 and CIS–250 are closer to the expected stoichiometric Cu/In and S/(Cu+In) ratios. Furthermore, the as-deposited samples did not show any peaks in their XRD patterns (not shown here), confirming the amorphous nature of the as-deposited samples. For applications in solar cells, annealing is normally performed to crystallize electrodeposited CIS films, which will improve the electron mobility, charge transport and reduce recombination at the interface between the absorbent and the buffer layer.

In this sense, CIS–150, CIS–200 and CIS–250 are the most suitable to be used as absorbent layers in solar cells (composition close to the stoichiometric one) and therefore only these samples were subjected to annealing.

3.3 Characterization of annealed samples

Figure 5 shows the SEM images for annealed samples (a–CIS–150, a–CIS–200 and a–CIS–250), where a decreased size of aggregates is observed when compared with the as-deposited samples (see Fig. 3), with sizes in the range of 1–2 μm. Since electrodeposition is a non-equilibrium technique used to obtain films, the decreasing size of aggregates could be a consequence of the surface diffusion and crystallization during the annealing process. It is also observed that the particle size tends to decrease as the LiCl concentration increases. This characteristic indicates that, as the LiCl concentration increases, the non-equilibrium conditions for CIS deposition augment, resulting in unstable larger size agglomerates that after annealing decrease in size. To explain this, we consider CIS–250 as an example: the as-deposited sample showed the largest size of agglomerates (Fig. 3(e)) and after annealing showed the lowest size of agglomerates (Fig. 5(c)). In addition, for all the annealed samples, some cracks were also seen, which can be attributed to residual stresses from the electrodeposition process.

The band gap values of the annealed samples were found to be between 1.42 and 1.49 eV, with no clear trend observed as a function of LiCl concentration. After annealing, a slight increase in the average band gap can be observed, which could be attributed to the appearance of the In_2O_3 phase discussed below (the band gap for In_2O_3 can be found between 3.0 and 3.5 eV [34,35]). In this sense, it has been reported that the presence of secondary phases with wider band gaps leads to a slight increase in the CIS band gap [36].

Figure 6 displays the XRD patterns for the annealed CIS samples. For all films, a strong peak located at $2\theta = 40.5°$ was observed, which is ascribed to the plane (1 1 0) of the cubic phase of Mo (Powder Diffraction File (PDF) N° 04–0809). Two other peaks are identified located at $2\theta = 27.87°$ and 46.31°, which are attributed to the reflection of the (1 1 2) and (2 0 4) planes, respectively, of the tetragonal phase of CIS according to PDF

N° 32–0339. Another peak close to 2θ = 55° can be observed, which is due to the contribution of two different peaks located at 54.73° and 55.09° ascribed to the (1 1 6) and (3 1 2) planes, respectively, of the tetragonal phase of CIS (see Fig. 7(a)). There are also two weak peaks positioned at 2θ = 30.48° and 52.76°, which correspond to the (2 2 2) and (4 3 3) planes, respectively, of the cubic In_2O_3 phase. The presence of secondary phases in electrodeposited CIS films has been previously reported and is a consequence of the annealing process [3,20].

A detailed inspection of the diffractograms reveals a reduction in the intensity of the peaks as the concentration of LiCl decreased. This is clearly seen in Fig. 7(b), where a reduction in the intensity of the (1 1 6) and (3 1 2) planes of the CIS phase as the LiCl concentration increases is observed. In order to estimate the crystallite size for the CIS phase, the Williamson-Hall analysis was carried out [37]. Figure 7(c) shows the crystallite size as a function of the LiCl concentration, where an increase in the crystal size is suggested. The supporting electrolyte has a direct impact on the electrolytic bath conductivity, with the higher the LiCl concentration, the greater the conductivity (and current density). It is known that in electrodeposition, the deposited mass is directly proportional to the current density. Therefore, as the LiCl concentration increases, a greater mass is deposited for the same deposition time. Thus, higher LiCl concentrations lead to morphological disorder that causes an increase in crystallite size after the annealing process.

3.4 ZnS/CIS bilayers for solar cell applications

The annealed CIS samples were used to fabricate bilayers for potential application in TFSC devices. Figure 8 shows the surface of the CIS films without and with the ZnS thin film layer. A change in the surface characteristics is clearly observed when the ZnS thin film is deposited on the surface of the CIS films. The ZnS thin films cover the surface of

the CIS layer, especially between the particles and aggregates (see red highlighted circles). Additionally, for all the obtained bilayers, it is also observed that ZnS deposition leads to an increase in the aggregate size. This can be clearly seen in a–CIS–250, where the aggregates size increased from 1.0–1.5 μm before ZnS deposition to 3.0–3.5 μm after ZnS deposition. This could be due to the higher growth rate of aggregates and larger particles, which act as preferential nucleation sites.

When comparing the surface characteristics of the three ZnS/CIS bilayers, it is possible to observe that the amount of aggregates tends to decrease for higher LiCl concentrations. This could be associated with the decreased particle size of the annealed CIS samples, as the LiCl concentration increases. Additionally, some cracks can be seen that could be related to the deposition rate that induces stress at the interface between ZnS and CIS [38].

The EDS analysis for the ZnS/CIS bilayers, summarized in Table 2, reveals the presence of small amounts of Zn, which is consistent with the expected film thickness (lower than 100 nm). No significant changes in the Cu/In and S/metal ratios were observed after the ZnS film deposition.

Concerning the ability of one-step electrodeposited CIS as an absorber layer in solar cells, the photovoltaic response of the ZnS/CIS bilayers were measured by recording the *J*–*V* curve under simulated solar radiation. Figure 9 shows the *J*–*V* curve for the ZnS/a–CIS–250 bilayer, which was the only sample that exhibited a photovoltaic response. This can be a consequence of the surface characteristics of annealed CIS samples and the low growth rates for ZnS thin films deposited from non-toxic solutions [39]. Since the particle size of a–CIS–250 sample is lower, this could lead to better coverage of ZnS and therefore the formation of a homogeneous bilayer. In this sense, further studies need to be carried out to find the experimental conditions that result in better coverage of ZnS on the CIS

surface. For instance, in the present work, deposition of ZnS thin films was performed at 75 °C and it was observed that deposition times higher than 90 min were impractical because of solution evaporation. Therefore, different paths could be evaluated to solve this issue, such as changes in reactant concentration, solution pH or deposition of ZnS in several layers (to increase the ZnS film thickness and coverage).

From Fig. 9, it can be determined that the best values for the photocurrent (J_{sc}) and open-circuit potential (V_{oc}) were quite low (J_{sc} below 10 μA/cm^2 and V_{oc} of 8.6 mV). The best fill factor value reached was 23.7% and the efficiency of the device was lower than 1%. The linear like behavior shown in the *J*–*V* curve may be observed for solar cells with lower values of FF and efficiency [40,41]. As for the low efficiency reported in the present article, is likely the result of several factors, for example, the presence of cracks on the surface has been reported as a detrimental characteristic in solar cells that reduces the J_{sc} in solar cells [42,43]. In addition, the low fill factor value indicates that there is still an opportunity to noticeable optimize the device manufacturing process. In spite of the low photovoltaic response of the ZnS/CIS bilayer obtained, it was shown that ZnS/CIS is a heterojunction that can convert solar energy into electricity. It should be noted that this is the first attempt to obtain a ZnS/CIS heterojunction, where the ZnS film was deposited by a non-toxic chemical solution and the CIS layer was grown using one-step electrodeposition.

4. Conclusions

CIS thin films with a chemical composition close to the stoichiometric one were obtained in this work using a one-step electrodeposition process. The effect of different LiCl concentrations as a supporting electrolyte was investigated and it can be concluded that higher concentrations of LiCl resulted in larger agglomerates of CIS and a Cu:In:S ratio

close to the stoichiometric composition for CIS films. After the annealing process, a reduction in the agglomerate size and a decrease in particle size as the supporting electrolyte concentration increased were observed. Regarding the structural properties after annealing, larger crystallite sizes were obtained because of the disorder as the LiCl concentration increased. Concerning the ZnS/CIS bilayer, it can be concluded that ZnS better covers the surface of the a–CIS–250 sample due to the smaller particle size. From photovoltaic characterization, it was shown that the bilayer system composed of a ZnS buffer layer synthesized by a non-toxic solution and a CIS absorbent layer prepared by one-step electrodeposition with a LiCl concentration of 250 mmol has potential for thin film solar cell applications.

Declarations

Fundings: This work was financially supported by the *Comisión Nacional de Ciencia y Tecnología* (CONICYT) through the project FONDECYT Iniciación 11160368 and Gobierno de Aragón–Fondo Social Europeo (E14 17R). Authors also acknowledge the use of Servicio General de Apoyo a la Investigación–SAI, Universidad de Zaragoza, Spain.

Conflict of Interest: The authors declare that they have no conflict of interest.

Availability of data and material: All data generated or analyzed during this study are included in this published article. For any other datasets generated during and/or analyzed during the current study are available from the corresponding author on reasonable request.

Code availability: Not applicable.

References

1. Störkel U, Argour M, Murrell C, Lewerenz H (2001) Electrochemical Treatment of $CuInS_2$. Thin Solid Films 387: 182–184.

2. Xu X, Wang F, Liu J, Ji J (2010) Effect of potassium hydrogen phthalate ($C_8H_5KO_4$) on the one–step electrodeposition of single-phase $CuInS_2$ thin films from acidic solution. Electrochim Acta 55: 4428–4435.

3. Tang Y, Ng Y, Yun J, Amal R (2014) Fabrication of a $CuInS_2$ photoelectrode using a single-step electrodeposition with controlled calcination atmosphere. Roy Soc Ch Adv 4: 3278.

4. Moreau A, Insignares C, Escoubas L, Simon J, Bermúdez V, Pérez A, Izquierdo V, Ruiz C (2015) Impact of Cu-Au type domains in high current density $CuInS_2$ Solar cells. Sol Energ Mat Sol C 139: 101–107.

5. Guo J, Chang G, Zhang W, Liu X, He Y (2016) Facile synthesis of $CuInS_2$ nanoparticles using different alcohol amines as solvent. Chem Phys Lett 647:51–54.

6. Abushama J, Rommel N, Johnston S, Ward S, Wu X (2005) Improved performance in $CuInSe_2$ and surface–modified $CuGaSe_2$ solar cells. Proceedings of the 31st IEEE Photovoltaic Specialists Conference, Lake Buena Vista, 299–302.

7. Green M, Hishikawa Y, Dunlop E, Levi D, Hohl J, Ho A (2018) Solar cell efficiency tables (version 51). Prog Photovoltaics 26: 3–12.

8. Goto H, Hashimoto Y, Ito K (2004) Efficient thin film solar cell consisting of TCO/CdS/$CuInS_2$/$CuGaS_2$ structure. Thin Solid Films 451–452: 552–555.

9. Nakabayashi T, Miyazawa T, Hashimoto Y, Ito K (1997) Over 10 % efficient $CuInS_2$ solar cell by sulfurization. Sol Energ Mat Sol C 49: 375–381.

10. Yuan J, Shao C, Zheng L, Fan M, Lu H, Hao C, Tao D (2014) Fabrication of $CuInS_2$ thin film by electrodeposition of Cu–In alloy. Vacuum 99: 196–203.

11. Zhuang M, Wei A, Zhao Y, Liu J, Yan Z, Liu Z (2015) Morphology controlled growth of special nanostructure $CuInS_2$ thin films on an FTO substrate and their application in thin film solar cells. Int J Hydrogen Energ 40: 806–814.

12. Peng S, Liang J, Zhang L, Shi Y, Chen J (2007) Shape–controlled synthesis and optical characterization of chalcopyrite $CuInS_2$ microstructures. J Cryst Growth 305: 99–103.

13. Bollero A, Trigo J, Herrero J, Gutiérrez M (2009) Simplified modulated evaporation process for production of $CuInS_2$ films with reduced substrate temperatures. Thin Solid Films 517: 2167–2170.

14. Cherian A, Jinesh K, Kashiwaba Y, Abe T, Balamurugan A, Dash S, Tyagi A, Kartha C, Vijayakumar K (2012) Double layer $CuInS_2$ absorber using spray pyrolysis: A better candidate for CuInS2/In2S3 thin film solar cells. Sol Energy 86: 1872–1879.

15. Di Iorio Y, Vázquez M (2017) Inexpensive methodology to prepare TiO_2/$CuInS_2$ hetero–junctions for photovoltaic applications. Mater Res Express 4: 045903.

16. Broussillou C, Andrieux M, Herbst M, Jeandin M, Jaime J, Morin S (2011) Sulfurization of Cu–In electrodeposited precursors for $CuInS_2$–based solar cells. Sol Energ Mat Sol C 95: S13–S17.

17. Lu L, Wang Y, Li V (2012) Influence of processing parameters on the preparation of $CuInS_2$ thin film by one–step electrodeposition as the solar cell absorber. Surf Coat Tech 212: 55–60.

18. Greenwood N, Earnshaw A (1997) Chemistry of the Elements (2^{nd} ed.). Butterworth-Heinemann. ISBN 0–08–037941–9.

19. Martínez A, Fernández A, Arriaga L, Cano U (2006) Preparation and characterization of Cu–In–S thin films by electrodeposition. Mater Chem Phys 95: 270–274.

20. Asenjo B, Chaparro M, Gutiérrez M, Herrero J (2006) Electrochemical growth and properties of $CuInS_2$ thin films for solar energy conversion. Thin Solid Films 511–512: 117–120.

21. Cheng K, Chiang W (2011) Effect of [Cu]/[Cu+In] ratio in the solution bath on the growth and physical properties of $CuInS_2$ films using one–step electrodeposition. J Electroanal Chem 661: 57–65.

22. Guan R, Cao L, Sun Q, Cao Y (2015) Effects of preparation conditions on the $CuInS_2$ films prepared by one–step electrodeposition method. J Nanomater 2015: ID678929.

23. Wang J (2006) Analytical Electrochemistry, 3^{rd} edition, Wiley, USA.

24. Nieszporek J, Gugala D, Nieszporek K (2019) The effect of supporting electrolyte concentration on Zinc electrodeposition kinetics from Methimazole solutions. Electroanalysis 31: 1141–1149.

25. Dhanwate V, Chaure N (2013) Effect of growth potential on the electrodeposition of CIS thin films. Appl Nanosci 2: 1–5.

26. Ribeaucourt L, Savidant G, Lincot D, Chassaing E (2011) Electrochemical study of one–step electrodeposition of copper-indium-gallium-alloys in acidic condition as precursors layers for Cu(In,Ga)Se_2 thin films solar cells. Electrochim Acta 56:6628–6637.

27. You R, Lew K, Fu Y (2014) Effect of electrodeposition potential on composition of $CuIn_{1-x}Ga_xSe_2$ absorber layer for solar cell by one–step electrodeposition. Int J Photoenergy 2014:478428.

28. Martínez A, Arriaga L, Fernandez A, Cano U (2004) Band edge determination of $CuInS_2$ thin films prepared by electrodeposition. Mater Chem Phys 88: 41–420.

29. Xu X, Wang F, Liu J, Park K, Fujishig M (2011) A novel one–step electrodeposition to prepare single–phase $CuInS_2$ thin films for solar cells. Sol Energy Mater Sol Cells 95: 791–796.

30. Wijesundera R, Siripala W (2004) Preparation of $CuInS_2$ thin films by electrodeposition and sulphurization for applications in solar cells. Sol Energ Mater Sol C 81: 147–154.

31. Rodríguez C, Sandoval M, Cabello G, Flores M, Fernández H, Carrasco C (2014) Characterization of ZnS thin films synthesized through a non–toxic precursors chemical bath. Mater Res Bull 60: 313–321.

32. Di Iorio Y, Berruet M, Schreiner W, Vázquez M (2014) Characterization of $CuInS_2$ thin films prepared by one–step electrodeposition. J Appl Electrochem 44: 1279–1287.

33. Rabeh M, Khedmi N, Fodha M, Kanzari M (2014) The effect of thickness on optical band gap and N-type conductivity of $CuInS_2$ thin films annealed in air atmosphere. Energy Proced 44: 52–60.

34. Sharma R, Mane R, Mn S, Han S (2009) Optimization of growth of In_2O_3 nano-spheres films by electrodeposition for dye-sensitized solar cells. J Alloy Compd 479: 840–843.

35. Henriquez R, Muñoz E, Dalchiele E, Marotti R, Martin F, Leinen D, Ramos J (2013) Electrodeposition of In_2O_3 thin films from dimethyl sulfoxide based electrolytic solution. Phys Status Solidi A 210: 297–305.

36. Liang W, Yanlai W, Wei Y, Jun Z, Jiangang X (2015) Effect of sulfurization time on the formation of $CuInS_2$ thin films. Rare Metal Mat Eng 44: 805–807.

37. Rodríguez C, Sandoval M, Saavedra R, Trejo C, De la Carrera F, Aragón L, Sirena M, Delplancke M, Carrasco C (2016) Comprehensive study of growth mechanism and properties of low Zn content $Cd_{1-x}Zn_xS$ thin films by chemical bath. Mater Res-Ibero-Am J 19: 1335–1343.

38. Hong J, Lim D, Eo Y, Choi C (2017) Chemical bath deposited ZnS buffer layer for $Cu(In,Ga)Se_2$ thin films solar cell. Appl Surf Sci 432: 250–254.

39. Agawane G, Shin S, Kim M, Suryawanshi M, Gurav K, Moholkar A, Lee J, Yun J, Patil P, Kim J (2013) Green route fast synthesis and characterization of chemical bath deposited nanocrystalline ZnS buffer layers. Curr Appl Phys 13: 850–856.

40. Valdés M, Berruet M, Goosens A, Vázquez M (2010) Spray deposition of $CuInS_2$ on electrodeposited ZnO for low-cost solar cells. Surf. Coat. Tech. 204: 3995–4000.

41. Dehghani M, Behjat A, Tajabadi F, Taghavinia N (2015) Totally solution-processed $CuInS_2$ solar cells based on chloride inks: reduced metastable phased and improved current density. J Phys D: Appl. Phys. 48:115304

42. Dhimish M, Holmes V, Mehrdadi B, Dales M (2017) The impact of cracks on the photovoltaic power performance. J Sci: Adv Mater Devices 2, 199–2009.

43. Ennemri E, Logerais P, Balistrou M, Durastanti J, Belaidi I (2019) Cracks in silicon photovoltaic modules: a review. J Optoelectron Adv Mater 21, 74–92.

List of Tables

List of Figure Caption

Fig. 1 Schematic representation of the fabrication of ZnS/CIS/Mo solar cells

Fig. 2 Cathodic polarization curve for the Cu^{2+}+In^{3+}+KHP+$S_2O_3^{2-}$+LiCl systems at different concentration of supporting electrolyte (pH = 2.5)

Fig. 3 SEM images for as-deposited samples grown with a) 50 mM, b) 100 mM, c) 150 mM, d) 200 mM and e) 250 mM of LiCl. f) Perfilometric scan of the as deposited CIS-100 sample

Fig. 4 DRS spectra of the as-electrodeposited CIS samples for different LiCl concentration

Fig. 5 SEM images for annealed $CuInS_2$ grown with (a) 150 mM, (b) 200 mM and (c) 250 mM of LiCl

Fig. 6 Diffractograms for annealed $CuInS_2$ films

Fig. 7 (a) Deconvolution of XRD peak corresponding to (1 1 6) and (3 1 2) planes, (b) close up of the XRD patterns between angles 53 ° to 56 ° , and (c) crystallite size for annealed $CuInS_2$ films

Fig. 8 Surface view of the annealed $CuInS_2$ samples without and with ZnS layer

Fig. 9 Current density-voltage (J–V) curve of ZnS/a–CIS–250 sample.

Table 1

Sample	Cu (at. %)	In (at. %)	S (at. %)	(Cu/In)	S/(Cu+In)
CIS-250	27.02	26.29	46.51	1.03	0.872
CIS-200	29.65	27.04	43.31	1.10	0.763
CIS-150	26.90	27.29	45.81	0.99	0.845
CIS-100	27.73	32.14	40.13	0.86	0.670
CIS-50	19.63	33.73	46.63	0.58	0.873

Table 1/2 C.A. Rodríguez et al

Table 2

Sample	Zn (at. %)	Cu (at. %)	In (at. %)	S (at. %)	(Cu/In)	(Sulfur/Metal)
ZnS/CIS-250	3.20	25.82	21.16	49.83	1.22	0.993
ZnS/CIS-200	1.16	25.79	25.89	47.21	0.996	0.893
ZnS/ CIS-150	5.22	23.06	24.82	46.90	0.929	0.883

Table 2/2 C.A. Rodríguez et al.

Figure 1-revised

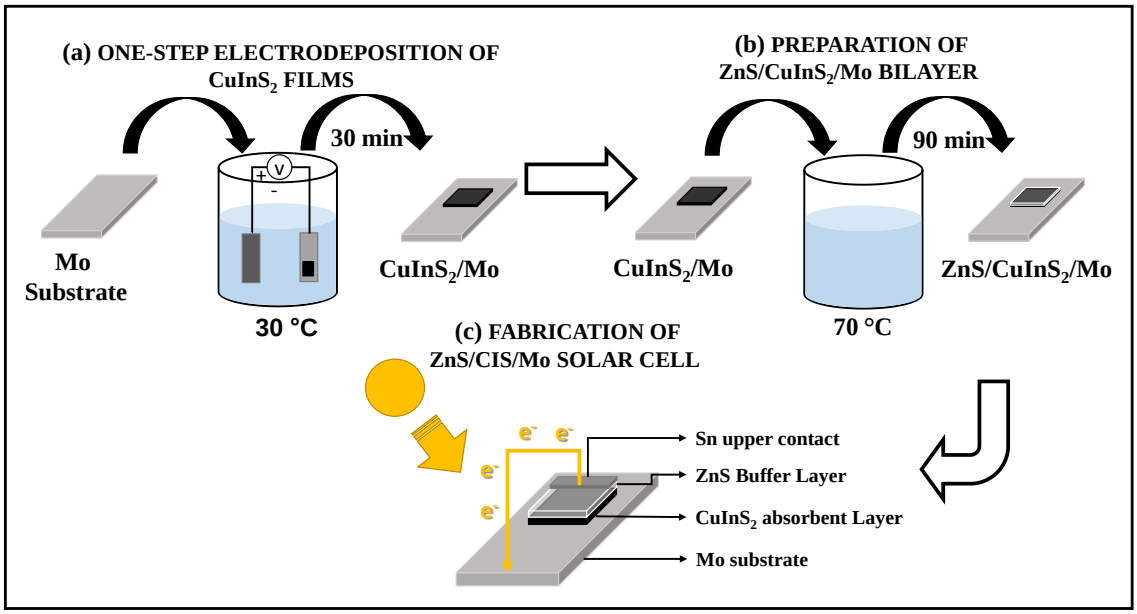

Figure 1/9 C.A. Rodríguez et al.

Figure 2-revised

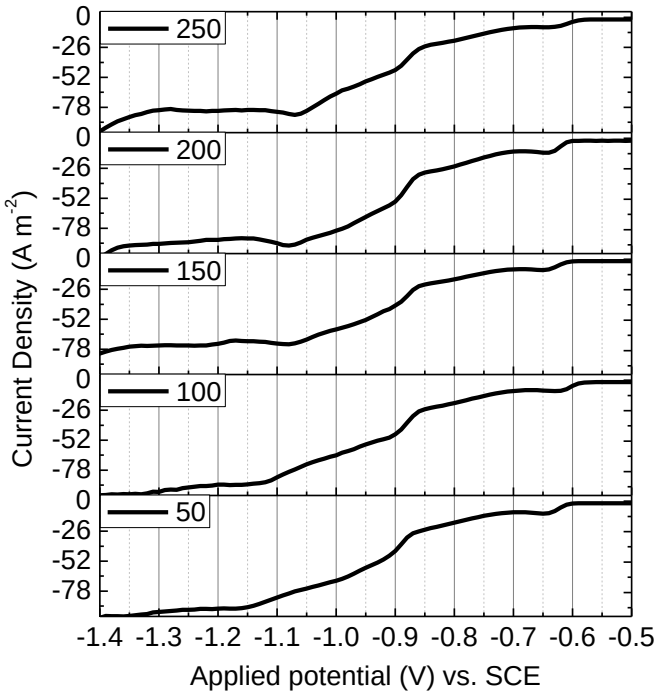

Figure 2/9 C.A. Rodríguez et al.

Figure 3-revised

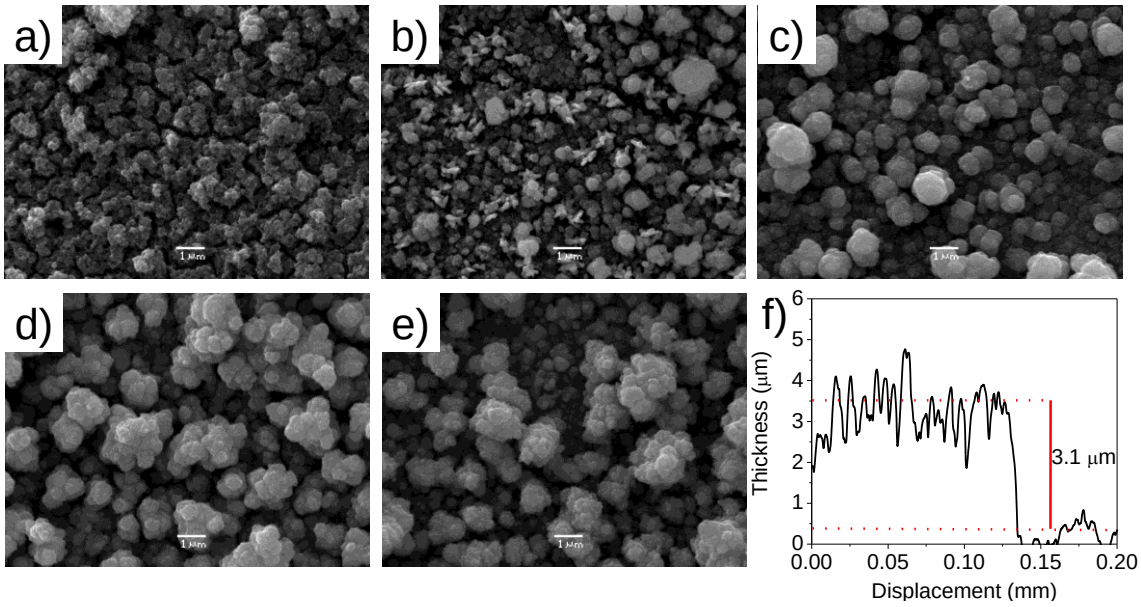

Figure 3/9 C.A. Rodríguez et al.

Figure 4-revised

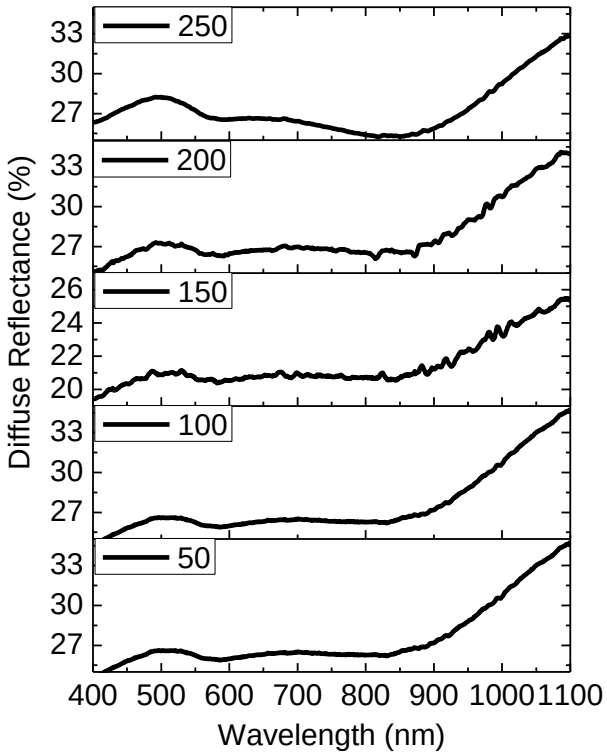

Figure 4/9 C.A. Rodríguez et al.

Figure 5a-revised

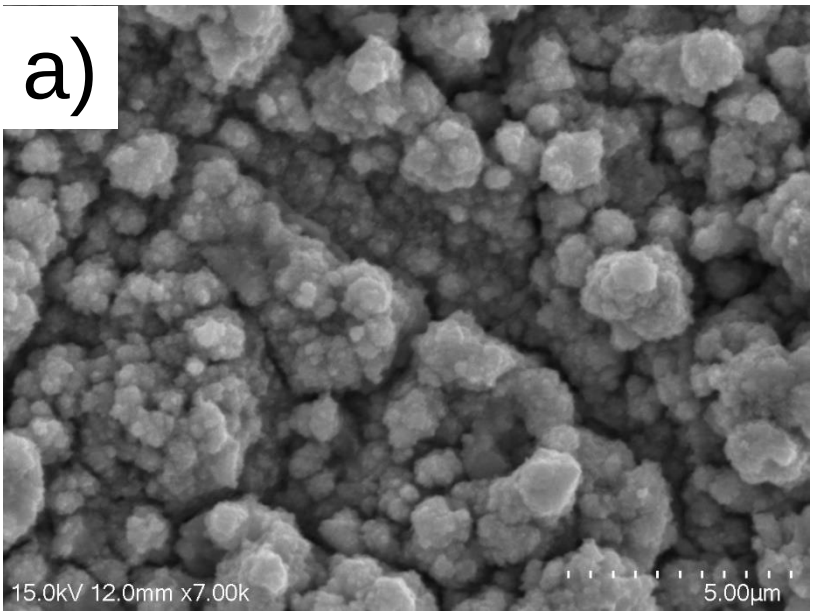

Figure 5 (a)/9 C.A. Rodríguez et al.

Figure 5b-revised

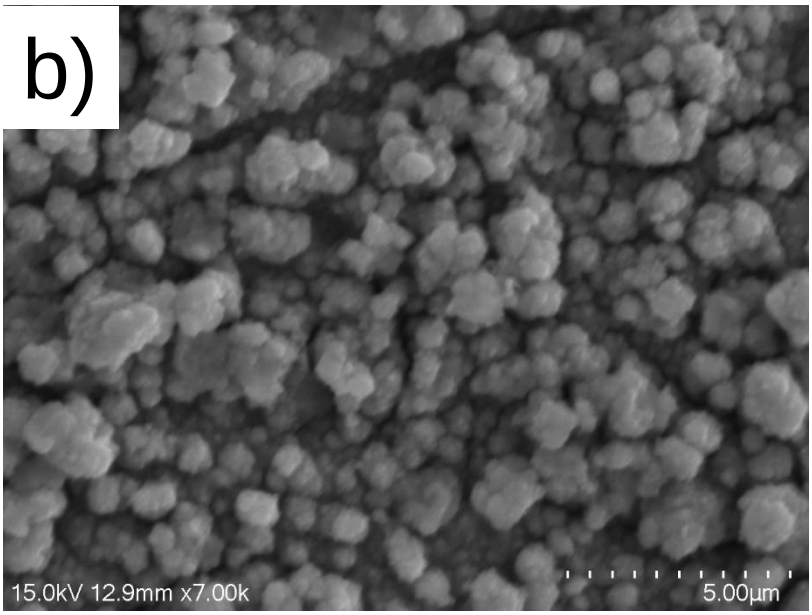

Figure 5 (b)/9 C.A. Rodríguez et al.

Figure 5c-revised

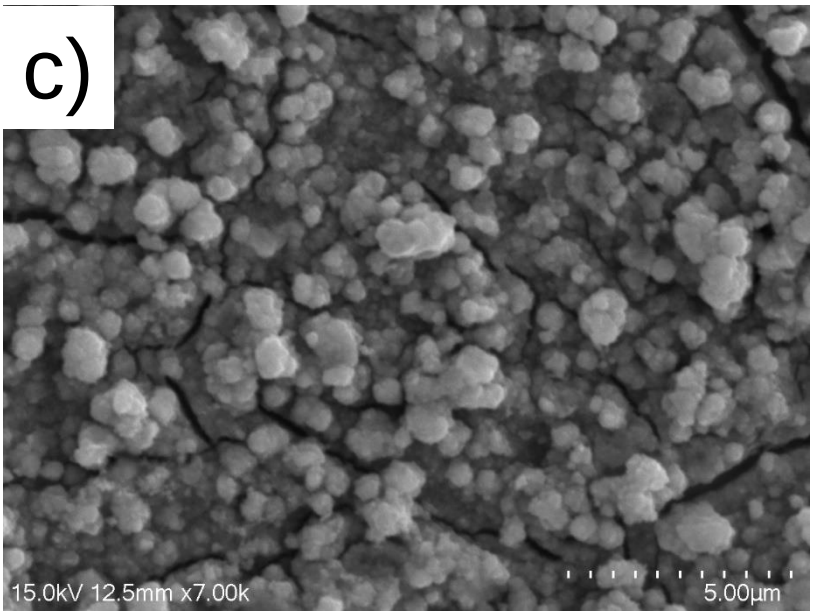

Figure 5 (c)/9 C.A. Rodríguez et al.

Figure 6-revised

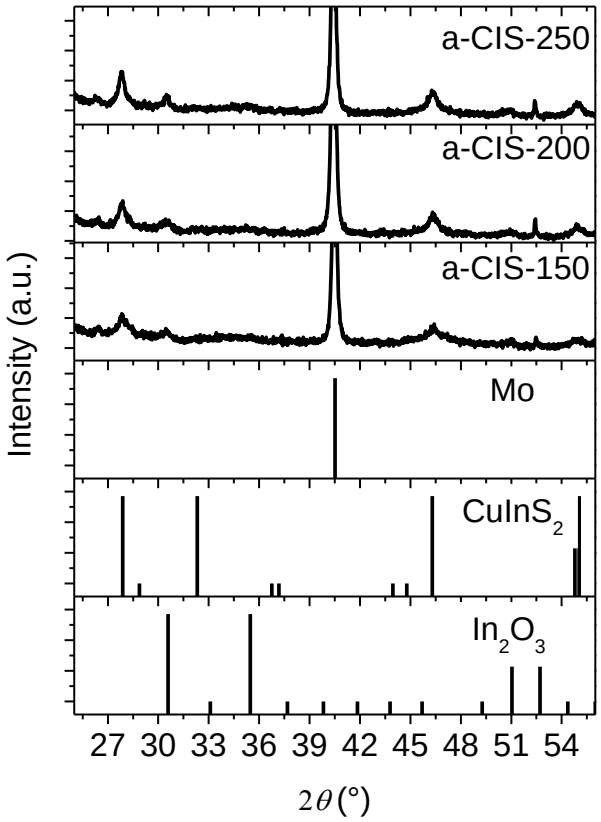

Figure 6/9 C.A. Rodríguez et al.

Figure 7a-revised

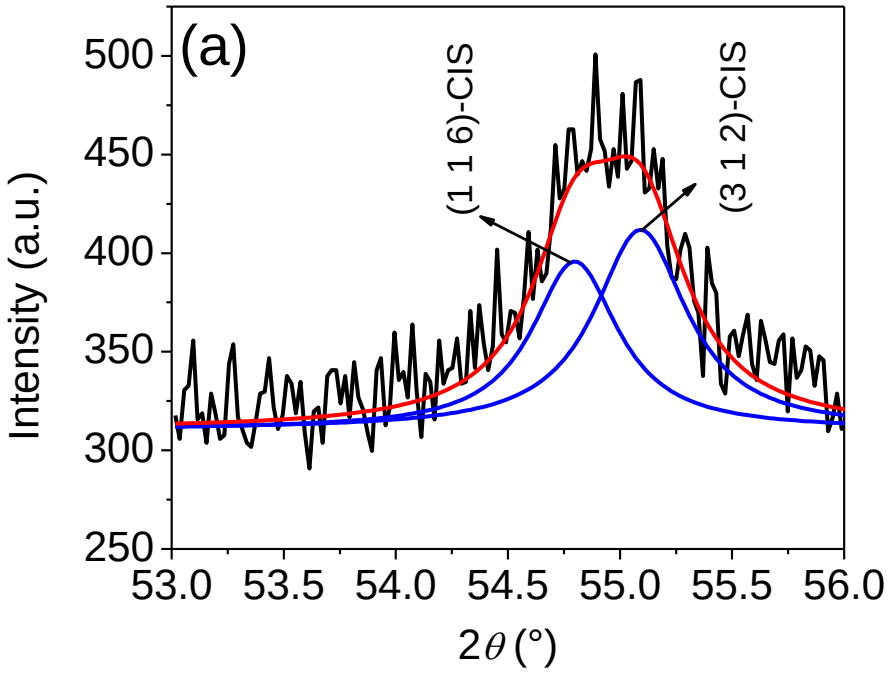

Figure 7 (a)/9 C.A. Rodríguez et al.

Figure 7b-revised

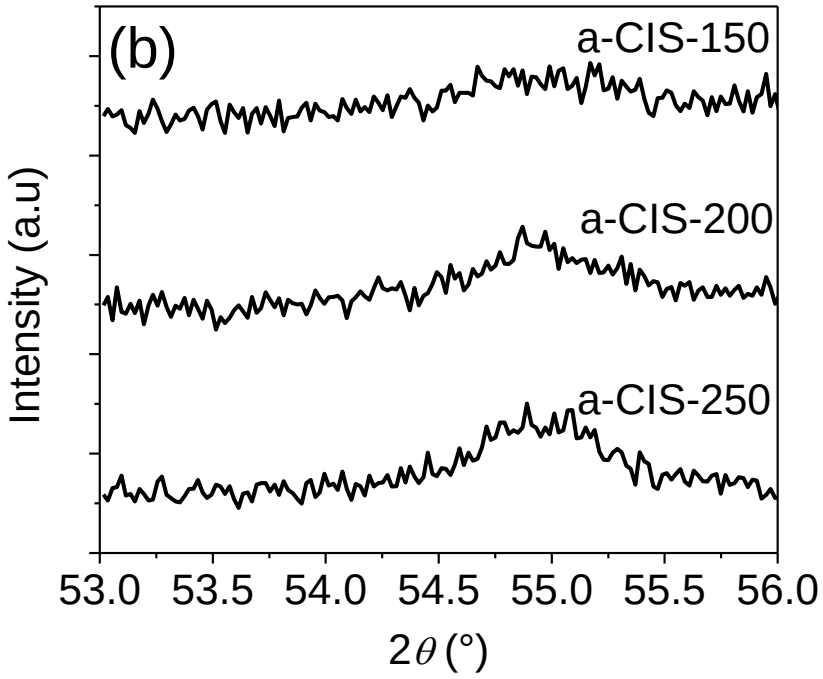

Figure 7 (b)/9 C.A. Rodríguez et al.

Figure 7c-revised

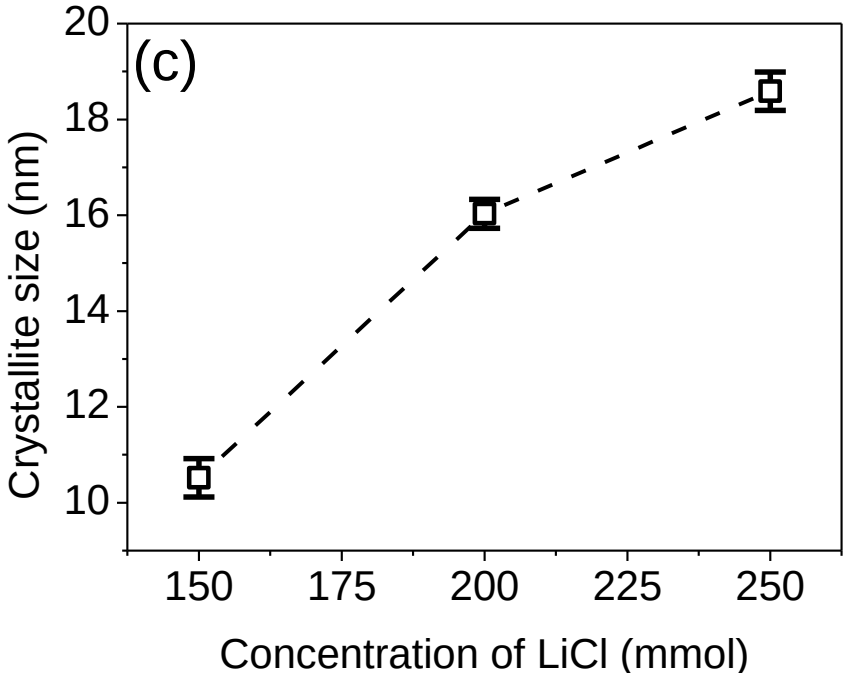

Figure 7 (c)/9 C.A. Rodríguez et al.

Figure 8-revised

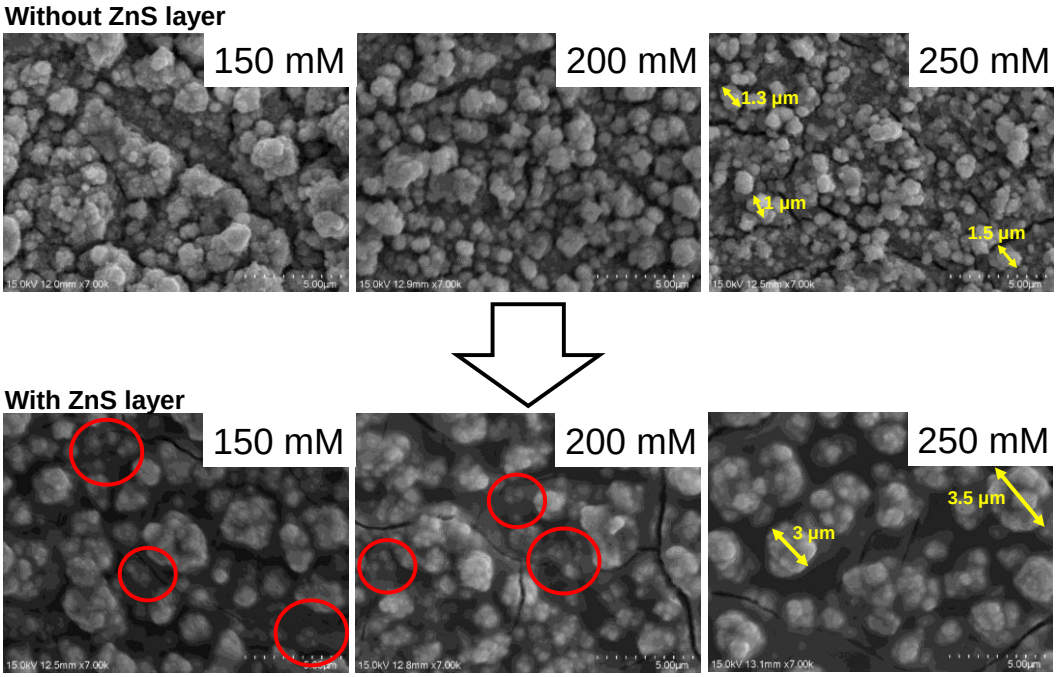

Figure 8/9 C.A. Rodríguez et al.

Figure 9-new

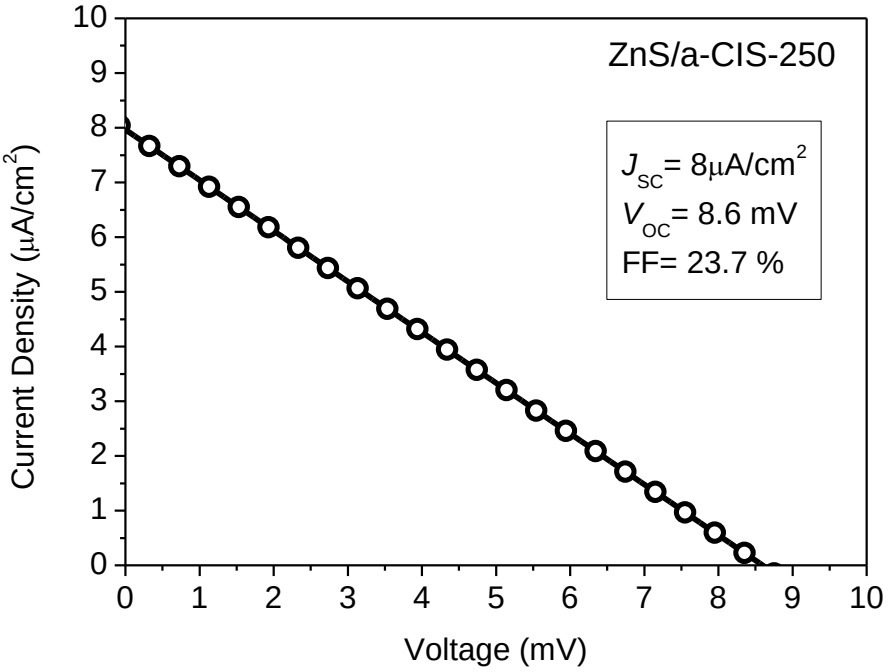

Figure 9/9 C.A. Rodríguez et al.